ADVANCED OPTICAL MATERIALS
www.advopticalmat.de

Shedding Light on the Mid-Infrared Complex Refractive Index of Anodic Aluminum Oxide

*Alba Díaz-Lobo, Irene Castro-Fernández, Eduardo Blanco, Daniel Ramos, Marisol Martin-Gonzalez, and Cristina V. Manzano**

In the current scientific landscape, the understanding of optical properties in the mid-infrared (mid-IR) range (3–30 µm) is crucial in simulations and models to explore the potential of materials for various applications. However, due to the challenges associated with mid-IR characterization, accurate refractive index (*n*) and extinction coefficient (κ) data are often lacking in the literature. This study addresses this gap by investigating the mid-IR *n* and κ spectra of anodic aluminum oxide (AAO) nanostructures anodized under different conditions, using two distinct approaches: IR ellipsometry and a theoretical model based on multilayer reflection and effective medium. The results demonstrate a strong agreement: the anodizing conditions have a significant influence on the optical properties of the AAO nanostructures. These differences enable accurate simulations of the emissivity spectra of AAO nanostructures on Al foils, which align closely with experimental measurements. This theoretical approximation is versatile and extensible to a broad range of materials. Different materials are tested, namely, a sapphire, a polycarbonate film, and a polyethylene terephthalate (PET) film achieving a useful qualitative description. This study paves the way for a novel approach in the engineering of new micro and nano-optical materials, facilitating their evaluation for suitability in mid-IR applications.

1. Introduction

Currently, applications involving mid-infrared (mid-IR) wavelengths (3-30 µm) are pivotal in various scientific,[1,2] industrial,[3–6] medical,[7,8] and security-related[9] fields. Notably, advancements in non-invasive diagnostic techniques using IR thermography, a non-contact thermometry technique capable of measuring the thermal characteristics of large surfaces areas[10] are particularly noteworthy.[11,12] However, the temperature cannot be directly read; instead, the infrared (IR) radiation emanating from the surface of interest must be interpreted as consisting of emitted, reflected, and transmitted IR radiation.

The emissivity of an object, which determines its optical properties in comparison with a black body, is closely related to passive daytime radiative cooling[13–15] (PDRC), a subject of considerable attention[16] in recent years. PDRC involves a material with optimized emissivity that reflects sunlight (0.3–2.5 µm) and radiate heat through the main atmospheric window (8-13 µm) toward the cold outer space.[17] This results in cooling without any power input, even under direct sunlight. As the Earth's atmosphere's main transparent region is in the mid-IR wavelength range, mid-IR characterization is critical to developing more efficient passive daytime radiative cooling materials.

In the recent years, several approaches to PDRC have been reported,[18–21] with porous materials[22–28] showing promising results. Multiple works have been reporting the use of porous Anodic Aluminum Oxide (AAO) nanostructures[27,29–36] (also known as nanoporous anodic alumina -NAA-, nanohole alumina arrays, or nanoporous anodized alumina platforms, -NAAP-). These nanostructures are cost-effective, environmentally friendly, and serve as useful templates for nanostructuring a wide variety of materials such as semiconductors,[37–39] metals[40] and polymers[41] Our recent work[27] shows that the passive cooling capability of AAO on Al foils depends on anodizing conditions, which modify the alumina thickness, the porosity grade, and the trapped counterions and so the emissivity spectrum. These changes must be considered in simulations and models to obtain reliable results.

A. Díaz-Lobo, M. Martin-Gonzalez, C. V. Manzano
Instituto de Micro y Nanotecnología
IMN-CNM
CSIC (CEI UAM+CSIC) Isaac Newton, 8, Tres Cantos, Madrid E-28760, Spain
E-mail: cristina.vicente@csic.es

I. Castro-Fernández, D. Ramos
Optomechanics Lab
Instituto de Ciencia de Materiales de Madrid (ICMM-CSIC)
3 Sor Juana Inés de la Cruz (Madrid), Madrid E-28049, Spain

E. Blanco
Departamento de Física de la Materia Condensada & IMEYMAT: Institute of Research on Electron Microscopy Materials
University of Cadiz
Puerto Real, Cádiz E-11510, Spain

The ORCID identification number(s) for the author(s) of this article can be found under https://doi.org/10.1002/adom.202401967

DOI: 10.1002/adom.202401967

The complex refractive index of AAO has been extensively studied from the visible to the near-IR (NIR) ranges (0.4 µm to 2.5 µm).[42–45] However, the current literature on the mid-IR range is insufficient for accurate performance. Further characterization is required to extend the data range to the mid-IR wavelengths. Ellipsometry can provide accurate results on a material's complex refractive index when the material is well known. However, due to the complexity of this analysis, few studies have addressed it.

In this work, we present an in-deep study where ellipsometric analysis have been used to obtain the mid-IR complex refractive index of AAO nanostructures anodized in different electrolytes, in a wide wavelength range from 3 to 30 µm. The selected electrolytes are four of the most commonly used in alumina anodization: phosphoric acid, oxalic acid, sulphuric acid, and ethylene glycol containing sulphuric acid.[46] The AAO nanostructures show different morphological properties, such as pore diameter (D_p) and interpore distance (D_{int}), depending on the electrolyte and the anodization conditions. Thus, the purpose of using several electrolytes is to study the influence of both the morphology and chemical structure on the n and κ in the mid-IR range.

Additionally, we propose a theoretical modeling based on multilayer reflection and effective medium to provide a quick approach of mid-IR complex refractive index. This can be used to assess the potential of a new material in the early stages of research to determine if the materials are suitable for target IR applications.

This model uses a multilayer system to get n and κ data from the experimental reflectance and transmission spectra[47–51] of a material. This approximation provides the mid-IR complex refractive index of free-standing AAO nanostructures from the reflectance and transmission of AAO on Al foil. Then, the obtained n and κ spectra by both ellipsometric analysis and approximation are compared and used to simulate the mid-IR emissivity spectra of the AAO nanostructures on Al foil anodized in the four different electrolytes. These simulations are performed by WVASE ellipsometric software from Woollam and COMSOL software. Finally, as a proof of concept about the potential of this theoretical approximation, it is used to analyzed a completely different material, such as a film of polyethylene terephthalate (PET). Therefore, mid-IR complex refractive index of PET is also obtained and compared with the ellipsometric analysis.

2. Experimental Section

2.1. Obtention of AAO Nanostructures Sapphire, Polycarbonate and PET Films

AAO nanostructures on Al foils were fabricated using a standard two-step anodization process in different electrolytes, as outlined in previous works.[27,52] The electrolytes employed included phosphoric acid (1 wt.% phosphoric acid + 0.01 M Al oxalate), oxalic acid (0.3 M oxalic acid), sulphuric acid (0.3 M sulphuric acid), and ethylene glycol containing sulphuric acid (50 wt.% ethylene glycol + 10 wt.% sulphuric acid). The duration of the second anodization was adjusted for each electrolyte to achieve an approximate thickness of 12 µm.

To fabricate free-standing AAO nanostructures, the Al foil was chemically etched using an aqueous solution of $CuCl_2$ and HCl. The barrier layer was then dissolved using an aqueous solution of phosphoric acid (10 wt.%, 85% Sigma-Aldrich) at 30 °C. To create patterned Al foil, the AAO layer was removed by a chemically etching in an aqueous solution of chromic oxide (1.8 wt.%, Sigma Aldrich) and phosphoric acid (7 wt.%, 85% Sigma Aldrich) at room temperature. **Figure 1** provides a schematic representation of the free-standing AAO nanostructures and the AAO nanostructures on the Al bulk.

Polycarbonate film with a thickness of 0.1 µm and polyethylene terephthalate (PET) film with a thickness of 100 µm were purchased from *Sterlitech* and *Goodfellow*, respectively. Single-crystal sapphire (Al_2O_3) with a thickness of 2 mm was purchased from *Marketech International*.

2.2. Morphological, Chemical Composition, and Optical Characterization

The morphological parameters of the AAO nanostructures were analyzed using a high-resolution Field Emission Scanning Electron Microscopy (FE-SEM, FEI VERIOS 460) with a 2 kV acceleration voltage. The top view images were digitally analyzed using XnView and ImageJ software to measure the pore diameter (D_p) and the interpore distance (D_{int}). Fast Fourier Transform (FFT) of collected FE-SEM top view images were obtained using the scanning probe image software WSxM 5.0.[53] The chemical composition of the AAO nanostructures was analyzed using Energy-dispersive X-ray (EDX), with an AMETEX EDAX detector, model Octane plus with 5 kV accelerating voltage. The EDX spectra of the AAO nanostructures are shown in Figure S1 (Supporting Information).

The surface roughness of the PET film was measured by atomic force microscopy (AFM) using a Bruker Dimension Icon microscope operating in non-contact mode with commercial probes from Nanosensors (type PPP-FM).

Mid-IR reflectance ($\boldsymbol{R}$) and transmission ($\boldsymbol{T}$) of free-standing AAO nanostructures, AAO on Al foil, and PET film, were measured from 2.5 µm to 17 µm using a Perkin Elmer Fourier Transform Infrared (FT-IR) spectrophotometer (Frontier), equipped with a 75-mm-diameter integrating gold sphere to collect the specular and diffuse reflectance components. The emissivity was calculated as $1 - \boldsymbol{R} - \boldsymbol{T}$.

Infrared Spectroscopic Ellipsometry (IRSE) measurements of free-standing AAO nanostructures and PET film were conducted on a Woollam IR-VASE Mark II ellipsometer, which integrates a Fourier-transform infrared (FTIR) interferometer source with a rotating compensator ellipsometer, ranging from 2.5 to 30 µm with a step size of 4 cm^{-1}. The ellipsometric angles Ψ and Δ spectra were obtained at three incidence angles of 50°, 60°, and 70° for the AAO nanostructures and for the patterned Al foil. Additionally, the transmission spectra were also measured for inclusion in the analysis. The optical model is described by a multilayer system formed by an air layer, a roughness layer, and the main material (AAO nanostructures or PET), which is considered a semi-infinite substrate. The experimental IRSE data were modeled using the WVASE (J.A. Woollam Co. Inc.) software package, version 3.942. The mid-IR emissivity of AAO

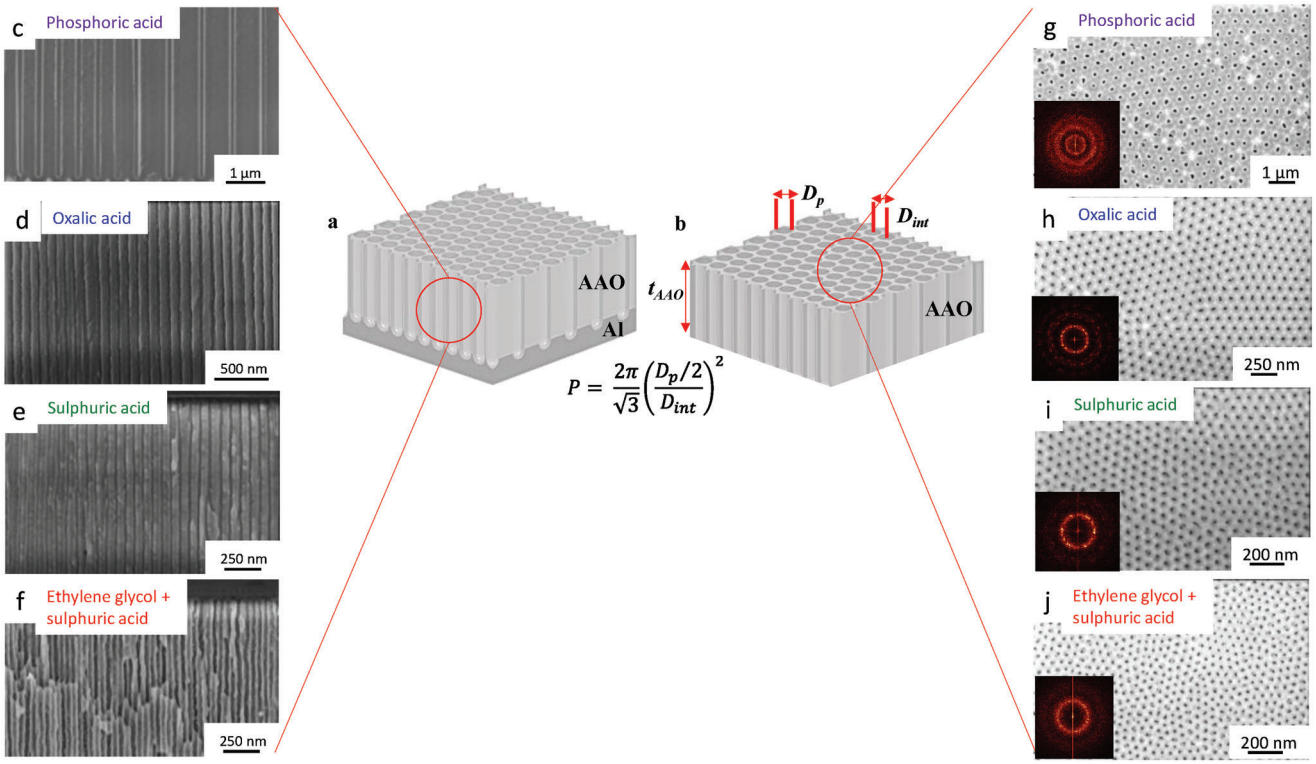

Figure 1. Schematic of the a) AAO nanostructures on Al bulk and and b) the free standing AAO nanostructures. The main morphological parameters have been highlighted: the pore diameter (D_p), the interpore distance (D_{int}), the alumina thickness (t_{AAO}), and the porosity (P). Cross-section FE-SEM view images of the AAO nanostructures when anodized in (c) phosphoric acid, d) oxalic acid, e) sulphuric acid, and f) ethylene glycol containing sulphuric acid. FE-SEM top view images of the AAO nanostructures surface when anodized in (g) phosphoric acid, h) oxalic acid, i) sulphuric acid, and j) ethylene glycol containing sulphuric acid. In the inset are the Fast Fourier Transform (FFT).

nanostructures over an Al foil was simulated by a multi-layer model using WVASE software, where the information about the thicknesses and the derived mid-IR complex refractive indices of the AAO nanostructure and the patterned Al foil were considered.

2.3. Theoretical Approximation of the mid-IR Complex Refractive Index

The model is composed of three stacked layers of materials (see Figure S3, Supporting Information). The first layer is air with complex refractive index $\tilde{n}_0 = n_0 = 1$. The second layer is material of interest (such as AAO nanostructure, PET or any other) with complex refractive index of $\tilde{n}_1 = n_1 + i\kappa_1$ and a thickness of d. The third layer is either an Al layer (in the case of the AAO nanostructures) with a complex refractive index $\tilde{n}_2$, the value of which is taken from the literature[54] or another air layer (in the case of PET).

An incident plane wave is assumed to propagate perpendicular to the surface, through the second layer, considering all possible reflections in the system. The accumulated phase on the material of interest is $k_0\tilde{n}_1 d$, where k_0 is the wave vector. The Fresnel reflection and transmission coefficients are denotated as $r_1, r_1', r_2, t_1t_1', t_2$, as shown in Figure S3 (Supporting Information). The Fresnel coefficients can be written as a geometric series, allowing a simple expression for the total reflection and transmission to be obtained:

$$t = \frac{t_1 t_2 e^{i\kappa_0 d n_1}}{1 - r_1 r_2 e^{2i\kappa_0 n_1 d}} \tag{1}$$

$$r = r_1 + \frac{r_2 t_1 t_1' e^{2ik_0\tilde{n}_1 d}}{1 - r_1' r_2 e^{2ik_0\tilde{n}_1 d}} \tag{2}$$

To obtain the values of the refractive index (n_1) and the extinction coefficient (κ_1) for the case of AAO nanostructures on Al foil, the transmission through the Al foil is assumed to be zero ($t_2 = 0$). For this case, only the difference between the theoretical and experimental reflectivity defined as a wavelength function $|R - R_{ex}| = f(n_1(\lambda),\kappa_1(\lambda))$ is minimized for each wavelength using a MATLAB code. The initial value for the refractive index is taken from the literature on alumina[55] and the initial value for κ_1 is derived from the transmission measurements taken without aluminum, T_{ex}, using the exponential decay of intensity as it propagates through a single layer:

$$\kappa_1 = -\frac{\lambda \log\left(T_{ex}\right)}{4\pi d} \tag{3}$$

In the case of PET, experimental values for both reflectance and transmittance are available, defining the function $|T - T_{ex}| =$

$f(n_1(\lambda),\kappa_1(\lambda))$. Thus, both functions are minimized to determine n_1 and κ_1, using as initial values the values of the optical constant closed to 3 µm taken from the experimental data of the literature.[56]

To fit these values to the Kramers-Kronig relations, a self-recurrent code is developed. This code implements the Kramers-Kronig Equations (4) and (5), introducing a weight to the initial calculated values, since the integrals are not calculated for all wavelengths, only for the measured ones. The Kramers-Kronig relations are fundamental in optical physics, linking the real and imaginary parts of a material's refractive index. These relations ensure that the calculated optical constants (refractive index, n, and extinction coefficient, κ) are physically consistent with the principle of causality. By implementing these relations in a self-recurrent code, we ensure that the derived values of n and κ are reliable and satisfy physical laws, providing a robust theoretical framework for understanding the material's optical behavior.

$$n\ (\lambda) = 1 + \frac{2}{\pi}\int_0^{\infty} d\lambda' \frac{\kappa\,(\lambda')}{\lambda'\left(1-\frac{\lambda^2}{\lambda'^2}\right)} \tag{4}$$

$$\kappa\ (\lambda) = \frac{2}{2\pi}\int_0^{\infty} d\lambda' \frac{1}{\lambda^2}\frac{n\,(\lambda')-1}{\frac{1}{\lambda'^2}-\frac{1}{\lambda^2}} \tag{5}$$

The layered model can exhibit limitations, specially at shorter wavelengths due to several factors. Increased scattering becomes significant at these wavelengths, as small particles and surface roughness within the layers scatter light more effectively. Additionally, interface roughness is more pronounced at shorter wavelengths, leading to increased diffuse scattering and deviations from the ideal reflections and transmissions described by Fresnel coefficients. Furthermore, the model assumes normal incidence, further complicating the accuracy at shorter wavelengths with different angles of incidence. These factors collectively reduce the model's ability to accurately describe the optical behavior of the system, especially in this range.

2.4. COMSOL Simulations of the mid-IR Emissivity

The commercially available electromagnetic waves module of the COMSOL Multiphysics finite element method (FEM) software was used to simulate the reflectance, the transmission, and consequently, the emissivity ($\varepsilon = 1 - R - T$) of AAO nanostructures on an Al foil and of PET film from the previously derived mid-IR complex refractive index. Analogous to the model used in section 2.3, the system was described as three stacked materials (air, material of interest, Al foil or air).

3. Results and Discussion

3.1. Analysis of the IR Complex Refractive Index of AAO Nanostructures

To understand how the optical properties of AAO nanostructures vary with the morphology and chemical structure, several AAO nanostructures were anodized in phosphoric acid, oxalic acid, sulphuric acid, and ethylene glycol containing sulphuric acid. All AAO nanostructures had a thickness of ≈12 µm. However, the complex refractive index, a property of the material, is not influenced by this parameter.

IR ellipsometric data were fitted over a broad wavelength range (3 to 30 µm) alongside normal-incidence optical transmission data. This approach was recently demonstrated[57] and provides a robust way to determine the IR complex refractive index. Integrating transmission data into the model fit is beneficial, as its complementary nature with ellipsometric data enables the acquisition of comprehensive information about transmitted light. Ellipsometry can accurately measure the thickness and refractive index of thin films, but it struggles to measure the extinction coefficient (κ) at very low values. By incorporating spectrophotometric measurements, the model's ability to determine such low κ values can be improved, as it is sensitive to changes in κ in regions of low absorption. Consequently, the fitting process included two datasets: infrared spectroscopic ellipsometry (IRSE) and IR transmission, which were analyzed together.

The optimal fitting of ellipsometric data for the free-standing AAO nanostructures required a surface roughness layer. We modeled this using the Bruggeman effective medium approach (BEMA) with 50% air and 50% alumina. The thicknesses of these surface roughness layers varied depending on the anodizing solution used: 205 nm for phosphoric acid, 28 nm for oxalic acid, 23 nm for sulphuric acid, and 8.5 nm for ethylene glycol-containing sulphuric acid.

Figure 2 shows the optimal fit achieved for the ellipsometric angle spectra, psi (Ψ) and delta (Δ), from 3 µm to 30 µm at incidence angles of 50°, 60°, and 70° and the normal-incidence transmission data. Ψ represents the amplitude ratio of the Fresnel reflection coefficients of the polarized light parallel (r_p), and perpendicular (r_s) to the incidence plane. Δ indicates the phase shift between the parallel and perpendicular components of the reflected light wave.

The WVASE software facilitates the derivation of the sample's imaginary component of the complex dielectric function using a linear combination of various numbers of oscillators within the so-called *GenOsc* layers to fit all the spectra. The configuration used include 9 Gaussians for AAO nanostructures anodized in phosphoric acid, 15 Gaussians for oxalic acid, 1 Cauchy + 4 Gaussians for sulphuric acid, and 11 Gaussians for ethylene glycol containing sulphuric acid. It is important to note that the oscillators change depending on the electrolyte in which the AAO nanostructures have been anodized. This is due to the incorporated ions into the AAO chemical structures, which provide different absorption bands.[27] The real part of the complex dielectric function is now calculated by the Kramers-Kronig integration formula, which is analogous to Equation (5). Both the real and imaginary part of the dielectric function are shown in Figure S4 (Supporting Information).

Dielectric materials are generally transparent at near-IR wavelengths. As seen in **Figure 3a**, the transmittance of the AAO nanostructures remains high, oscillating between 0.80 and 0.95 up to wavelengths near 6 µm when the anodization was performed in oxalic acid, sulphuric acid, or ethylene glycol

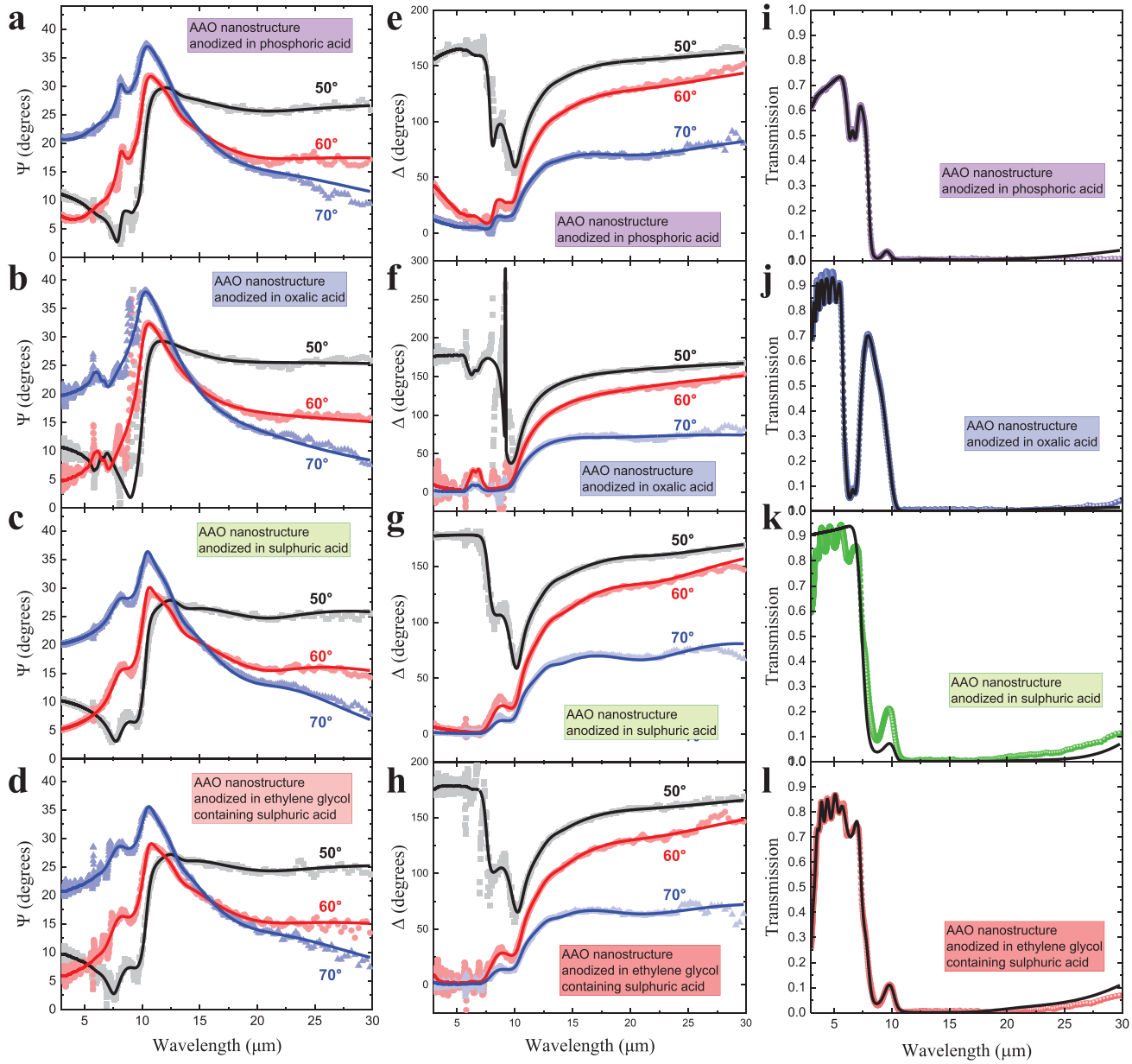

Figure 2. Experimental measurements and fit achieved for the ellipsometric angles at different incidence angles: a–d) Ψ and e–h) Δ of the free-standing AAO nanostructures at the same point where the i–l) optical transmission was measured for the AAO nanostructures anodized in the four different electrolytes.

containing sulphuric acid. In contrast, when the anodization was carried out in phosphoric acid, the maximum transmittance is 0.73 at 6 μm.

Then, at 7 μm, there are local maxima for the AAO nanostructures anodized in sulphuric acid and ethylene glycol containing sulphuric acid, and local minima for the ones anodized in phosphoric acid and oxalic acid. Before becoming opaque, one last transmittance peak appears in the 10 μm wavelength range for the AAO nanostructures anodized in phosphoric acid, sulphuric acid and ethylene glycol containing sulphuric acid. In the case of oxalic acid, this peak is shifted to 8 μm. This information was included in the model and, consequently, the deduced absorption coefficient (Figure 3b) of the AAO nanostructures differs slightly.

In accordance with the refractive index database[54] a crystal α-Al_2O_3 (sapphire) analyzed in the IR wavelength range should have an average value of the absorption coefficient of $(6.8 \pm 1.3)\cdot10^2$ cm^{-1} from 3 to 8 μm, $(9.4 \pm 3.7)\cdot10^2$ cm^{-1} from 8 to 11 μm, and $(1.1 \pm 0.3)\cdot10^4$ cm^{-1} from 11 μm to 13 μm. Therefore, for wavelengths from 3 to 7 μm, which are shorter than the atmospheric window, the average absorption coefficient of the AAO nanostructures is lower than the reported for the α-Al_2O_3 when the anodization is performed in sulphuric acid, $(1.4 \pm 0.3)\cdot10^2$ cm^{-1}, and in ethylene glycol containing sulphuric

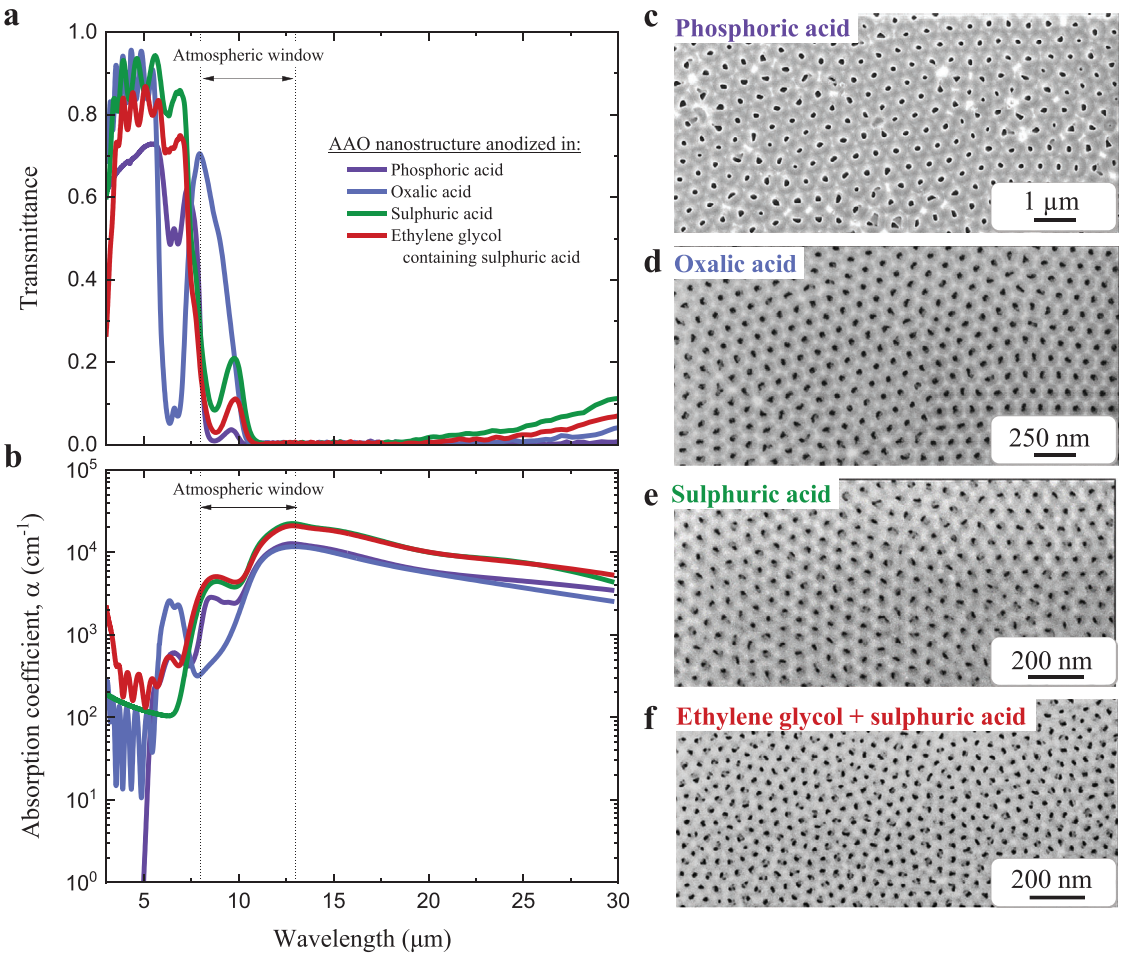

Figure 3. a) Normal incidence optical transmittance of the free-standing AAO nanostructures, b) absorption coefficient deduced from ellipsometry model, and FE-SEM top view images of the AAO nanostructures surface when anodized in (c) phosphoric acid, d) oxalic acid, e) sulphuric acid, and f) ethylene glycol containing sulphuric acid.

acid, $(3.6 \pm 1.8)\cdot10^2$ cm^{-1}. Meanwhile, the AAO nanostructures anodized in oxalic acid have an average absorption coefficient of $(9.5 \pm 6.8)\cdot10^1$ cm^{-1} from 3 μm to 5.5 μm and reach local maximum of $2.5\cdot10^3$ cm^{-1} at 6.5 μm. The AAO nanostructures anodized in phosphoric acid show a negligible absorption up to 5 μm and reach local maximum of $6.0\cdot10^2$ cm^{-1} at 6.5 μm.

For the wavelengths in the range of the atmospheric window, between 8 and 13 μm, the AAO nanostructures anodized in sulphuric acid and ethylene glycol containing sulphuric acid show very similar spectra, reaching maxima of $2.2\cdot10^4$ cm^{-1} at 12.5 μm, exceeding the value of the α-Al_2O_3. It is noteworthy that the AAO nanostructure anodized in oxalic acid shows an absorption coefficient significantly lower than the others between 8 and 10 μm. Then, the absorption coefficient peaks for the AAO nanostructures anodized in phosphoric acid and oxalic acid, $1.3\cdot10^4$ cm^{-1} at 12.5 μm, matching the average value of the α-Al_2O_3.

These spectral differences will remarkably impact the performance in passive radiative cooling applications[27] because the use of different anodization conditions leads to changes in the morphology and in the chemical structure. Regarding to the morphology, the Figure 3c-f shows the FE-SEM top view images of the AAO nanostructures anodized in four different electrolytes for 12 μm in thickness. Differences in the pore diameter (D_p) and the interpore distance (D_{int}) can be observed. The averages of D_p and D_{int} are 125 ± 25 and 480 ± 22 nm, 37 ± 4 and 104 ± 7 nm, 23 ± 3 and 68 ± 5 nm, and 16 ± 3 and 50 ± 10 nm for the AAO nanostructures anodized in phosphoric acid, oxalic acid, sulphuric acid, and ethylene glycol containing sulphuric acid, respectively.

The mid-IR (3 -30 μm) refractive index (n) and the extinction coefficient (κ) derived from the ellipsometric analysis for the free-standing AAO nanostructures anodized in the different electrolytes are shown in **Figure 4**.

The real part of the complex refractive indices, denoted n, and the extinction coefficient κ, are plotted in solid lines with distinct colors for every electrolyte: purple for phosphoric acid, blue for oxalic acid, green for sulphuric acid, and red for ethylene glycol containing sulphuric acid.

The n spectra for the different electrolytes show minor differences. AAO nanostructures anodized in oxalic acid reach a

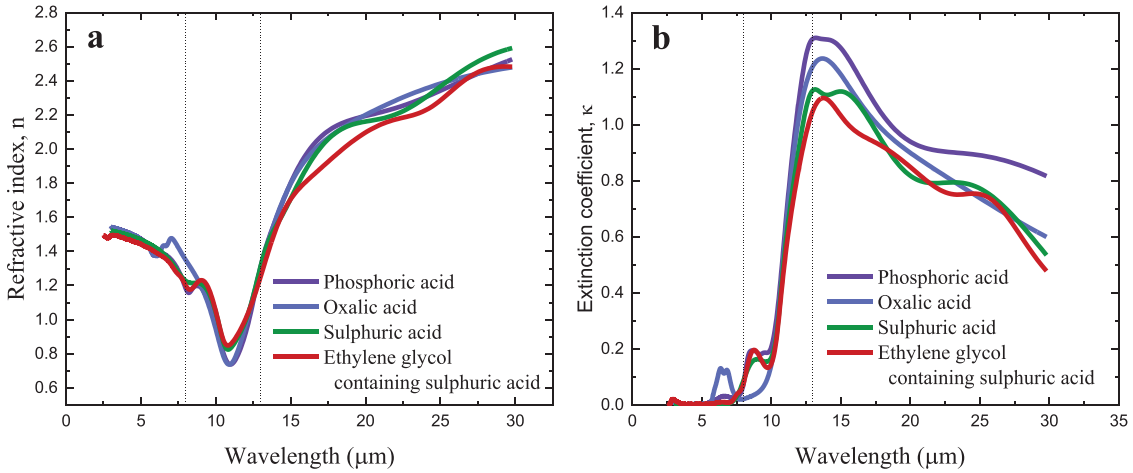

Figure 4. a) Refractive index and b) extinction coefficient deduced by ellipsometry analysis of AAO nanostructures anodized in phosphoric acid, oxalic acid, sulphuric acid, and ethylene glycol containing sulphuric acid.

local maximum of 1.47 at 7 μm. In contrast, those anodized in phosphoric acid, sulphuric acid, and ethylene glycol show local minimum of 1.16, 1.22, and 1.18 at 8.2 μm, respectively. All AAO nanostructures have an absolute minimum of the n value at 10.9 μm and an absolute maximum ≈2.5 at 30 μm.

The κ spectra, however, reveal significant differences among electrolytes. Two major features are apparent: the first at wavelengths shorter than 10 μm, and the second between 12 and 16 μm. The first local maximum for nanostructures anodized in phosphoric acid, sulphuric acid, and ethylene glycol containing sulphuric acid is ≈8.5 μm, while for those anodized in oxalic acid, it appears at 6.4 μm.

The second maxima ≈13.7 μm which attains different values for each electrolyte, peaking at 1.3 for phosphoric acid, 1.2 for oxalic acid, and 1.1 for both sulphuric acid and ethylene glycol containing sulphuric acid. These variations in absorption peaks are primarily due to two factors: first, the different counterions from the electrolytes incorporated into the alumina's chemical structure[30] and, second, the diameter and the interpore distance of the nanopores, which enhances the effective surface roughness and increases scattering processes. Note that all the AAO nanostructures have a porosity of ≈10%, despite the changes in pore diameter and interpore distance.[30]

The mid-IR complex refractive index of the AAO nanostructure anodized in oxalic acid aligns with behaviors previously reported from 3 to 15 μm[34] where n ranges from 1.5 to 1.75, reaching a minimum value of 0.7 at 11 μm, and κ ranges from 0 to 1.25. For AAO nanostructures anodized in sulphuric acid, the mid-IR refractive index is comparable to findings reported between 1 μm and 15 μm[58] with n ranging from 1.6 to 1.7 and a minimum of 0.65 at 11 μm, while κ ranges from 0 to 0.25 at 15 μm. The derived mid-IR κ spectra presented in this study show increased absorption, peaking at 1.1 at 15 μm. To the best of the author's knowledge, there is no published literature on the mid-IR complex refractive index of AAO nanostructures anodized in phosphoric acid and ethylene glycol containing sulphuric acid. These small variations in the mid-IR complex refractive index are relevant to IR applications, such has been demonstrated for passive radiative cooling.[27] These tiny changes significantly affect the cooling performance of the AAO nanostructures, either enhancing or limiting their cooling capability.

3.2. Theoretical Calculation of the mid-IR Complex Refractive Indices of AAO Nanostructures

To circumvent the challenges of IR ellipsometric analysis, a theoretical modeling based on multilayer reflection and effective medium is used to estimate the mid-IR complex refractive index of the AAO nanostructures anodized in the four different electrolytes. This approximation can obtain the n and κ spectra of the free-standing AAO nanostructures from the optical characterization of the AAO nanostructures on Al foil. As shown in **Figure** 5a-d, the only required input data are the reflectance spectra and the thickness of the alumina layers. The transmission through the Al layer is neglectable in all cases.

The comparison between the n and κ spectra obtained by both this approximation and the ellipsometric analysis are shown in Figure 5e-h for the four different electrolytes. The approximated n and κ spectra are plotted with shadow regions, representing an uncertainty in the thickness of the alumina of ± 1 μm. This variation in the alumina thickness was included in each calculation to investigate the stability of the model with respect to thickness variations.

The results of this approach show a moderate amount of noise associated with thickness variations and align well with the ellipsometric analysis. However, some discrepancies in n can be observed: a shift of ≈0.2 overestimates the values from 3 to 10 μm, a sharp minimum at 11 μm, and an overestimating of the values between 0.2 and 0.4 from 13 to 16 μm. Meanwhile, slight differences exist between the κ spectra. The differences can be attributed to the simplifications assumed in the theoretical approach, where neither surface roughness nor the effect of the barrier layer has been considered.

Taking all this into account, it can be concluded that the n and κ spectra provided by the approximation are valuable and readily accessible results. They can be quickly obtained and

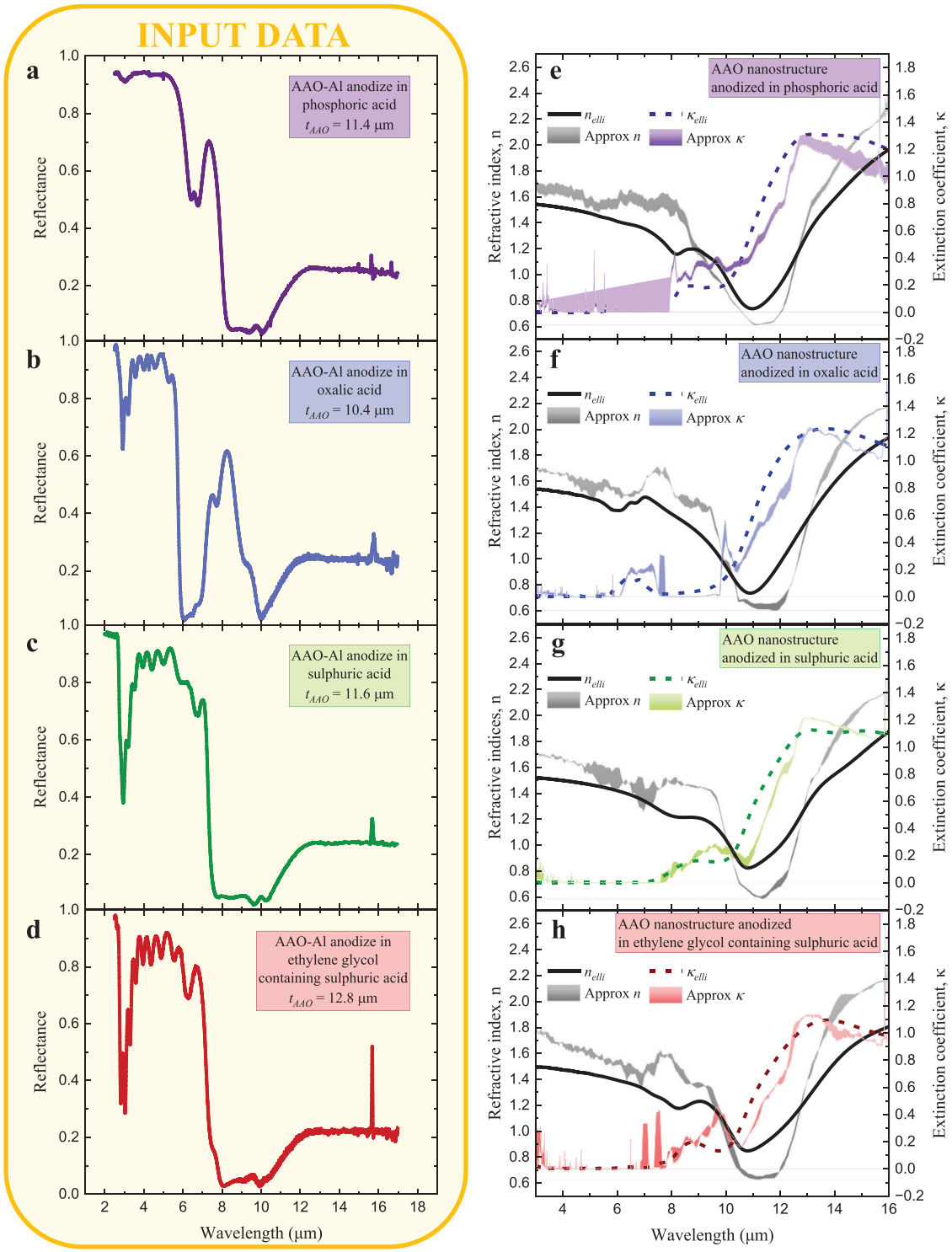

Figure 5. a–d) Input data for the theoretical approximation, which consist of IR reflectance spectra and AAO thickness of the AAO nanostructures on the Al foil. e–h) Mid-IR complex refractive index for the free-standing AAO nanostructures anodized in the different electrolytes: areas cover the ranges obtained by the model. The lines show the refractive index and the extinction coefficient deduced previously by ellipsometric analysis.

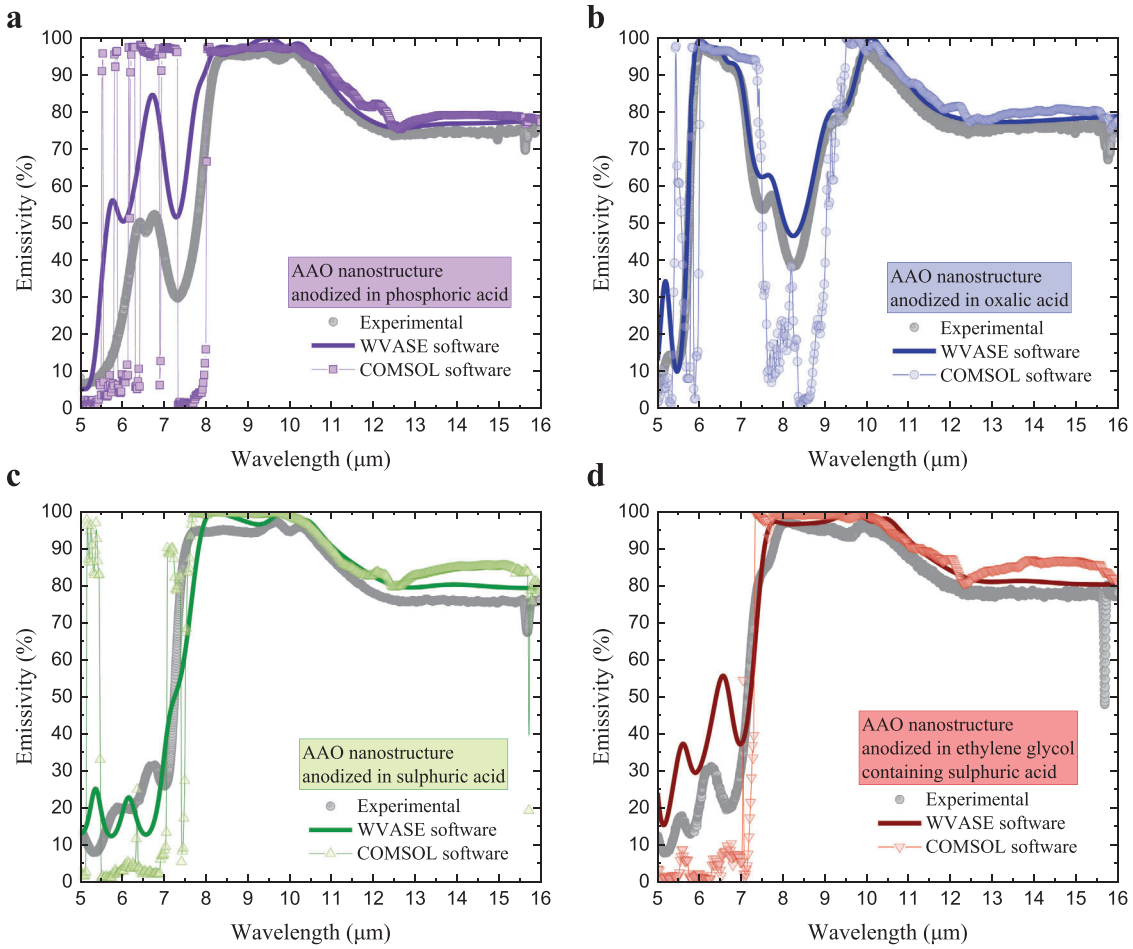

Figure 6. Emissivity of AAO nanostructures on Al bulk with an alumina thickness ≈12 μm anodized in different electrolytes: a) phosphoric acid, b) oxalic acid, c) sulphuric acid, and d) ethylene glycol containing sulphuric acid. Experimental data are shown with a scattered grey line, simulation by WVASE software with solid line and by COMSOL software with solid lines and symbols.

show a strong agreement with the results of the IR ellipsometric analysis.

3.3. Emissivity Spectra of AAO Nanostructures on Al Foils

The mid-IR complex refractive index data enables the modeling of critical properties such as mid-IR emissivity, which is of significant interest in passive radiative cooling applications. Therefore, the obtained n and κ spectra of the AAO nanostructures anodized in the four electrolytes are now used to model the mid-IR emissivity of these AAO nanostructures on Al foil.

Two approaches are followed: first, via ellipsometry, using WVASE software to model the reflectance of a multilayer system consisting of the patterned Al layer (see Figure S5, Supporting Information), the AAO layer, and a roughness layer on top with the values previously found during the ellipsometric analysis. Second, the electromagnetic waves module of COMSOL software is used to simulate the reflectance of a multilayer system of air, AAO layer, and Al foil. As the transmission through the Al foil is neglectable, the emissivity can be calculated as $1 - R$.

Figure 6 presents the results of both simulations along with the experimental data of the mid-IR emissivity of the AAO nanostructures on Al bulk anodized in the four different electrolytes.

Some differences in the fitting quality appeared when comparing AAO nanostructures on the Al foil anodized in the distinct electrolytes. In the cases of phosphoric acid, sulphuric acid, and ethylene glycol containing sulphuric acid, two regions can be distinguished: from 5 to 8 μm and from 8 to 16 μm. In the first region, the roughness of the surface and the characteristic dimensions of the AAO nanostructures are comparable to the wavelength. Therefore, the associated error related to neglecting these parameters will significantly affect the results; especially, in the case of phosphoric acid, which provides the largest pore diameter and interpore distance. Further details on error analysis, including residual and mean square error (MSE) analysis of both the mid-IR complex refractive index and the emissivity spectrum simulations, are provided in the Supporting Information (Figures S6 and S7; Tables S1 and S2, Supporting Information).

The COMSOL simulation is noisier in this wavelength range than the WVASE simulation, where the roughness was considered. The discrepancies between the WVASE simulation and the experimental data are related to the low extinction coefficient of

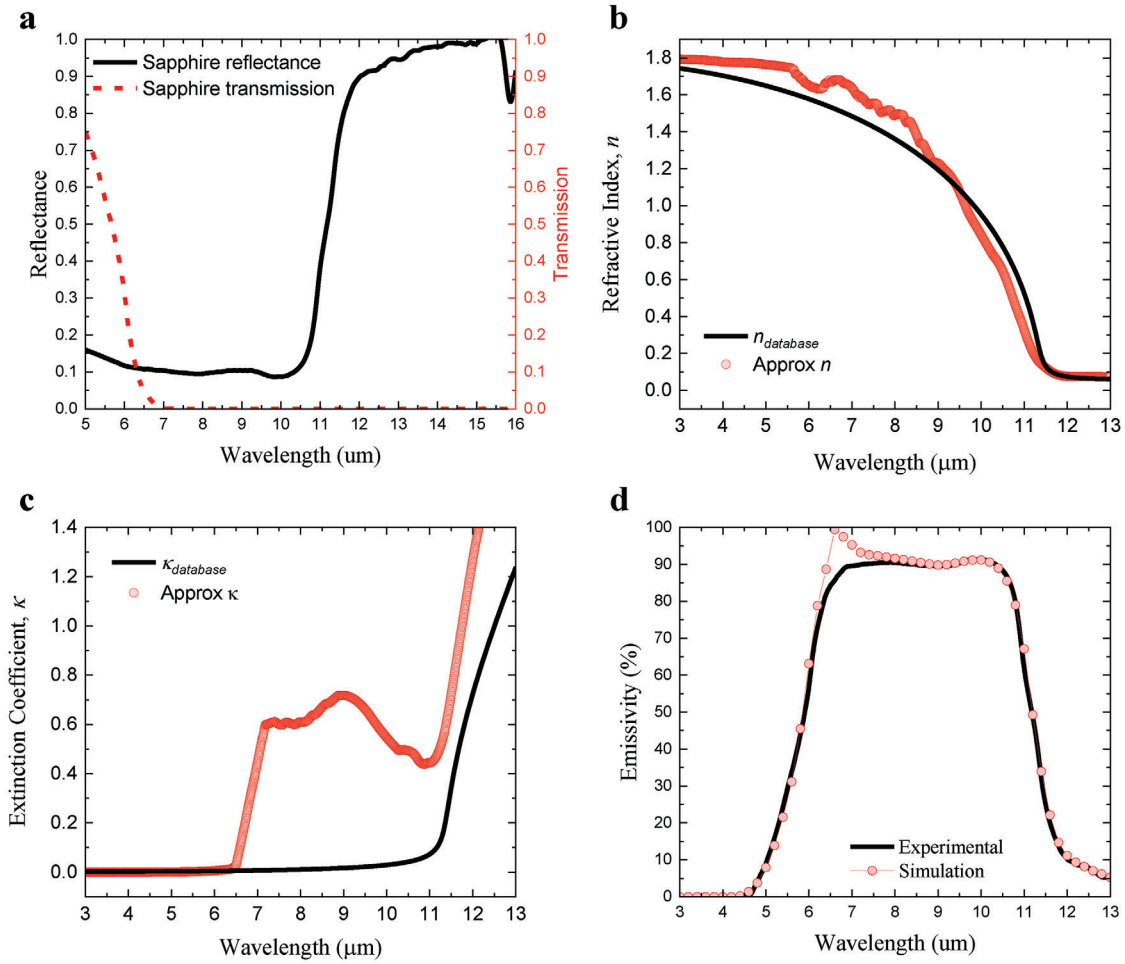

Figure 7. a) Optical characterization of reflectance and transmission spectra of a sapphire with a thickness of 2 mm. First approach to the mid-IR b) refractive index and c) extinction coefficient spectra of the sapphire provided by the theoretical approximation along with the reference spectra. d) Simulation of the emissivity spectrum using this approach to n and κ spectra with COMSOL software, along with the experimental measurement.

the AAO nanostructures in this range, as the ellipsometric analysis loses accuracy under these conditions. In the second region, a great fitting of the experimental data is achieved by both simulations.

Meanwhile, when the anodization is performed in oxalic acid, the COMSOL simulations overestimates the absorption due to the oxalate ions inside Al have absorption ≈8 μm[27] but the general fitting achieved from the approximation of n and κ is in great agreement with the experimental data.

3.4. Applicability of the Theoretical Approximation to Other Materials

In order to demonstrate the applicability of the theoretical approximation presented above, to explore its limits, and to assess the quality of the provided n and κ spectra, we selected several materials, namely: sapphire, as single-crystal Al_2O_3 and as example of transparent metal oxide; polycarbonate as porous polymer; and polyethylene terephthalate (PET) as a non-porous polymer. Both polymers have high mid-IR emissivity, thus their n and κ spectra have several peaks in this wavelength range, presenting a challenge to the model.

Similar to the steps followed above, the required optical properties for the theoretical approach are exclusively the reflectance and the transmission spectra of the material, which are directly measured using a Fourier Transform IR (FT-IR) spectrophotometer. The model used this input to generate an initial approximation of the mid-IR refractive index and the extinction coefficient of the material. To assess the quality of this initial approximation of n and κ, these spectra were used to simulated the emissivity spectrum of each material with COMSOL software. **Figure 7** shows the analysis of a sapphire with a thickness of 2 mm.

The mid-IR reflectance of the sapphire remains ≈0.1 from 5 to10.5 μm, it increases up to 0.9 at 11.5 μm and remains between 0.9 and 1.0 up to 16 μm. The mid-IR transmission decreases from 0.75 to 0.0 from 5 to 7 μm and remains around zero from 7 to 16 μm. These data allow the model to approximate the behavior of the refractive index (Figure 7b) and the extinction coefficient (Figure 7c) of the sapphire. Using the WVASE software database as a reference, the first approach for n describes a good fit

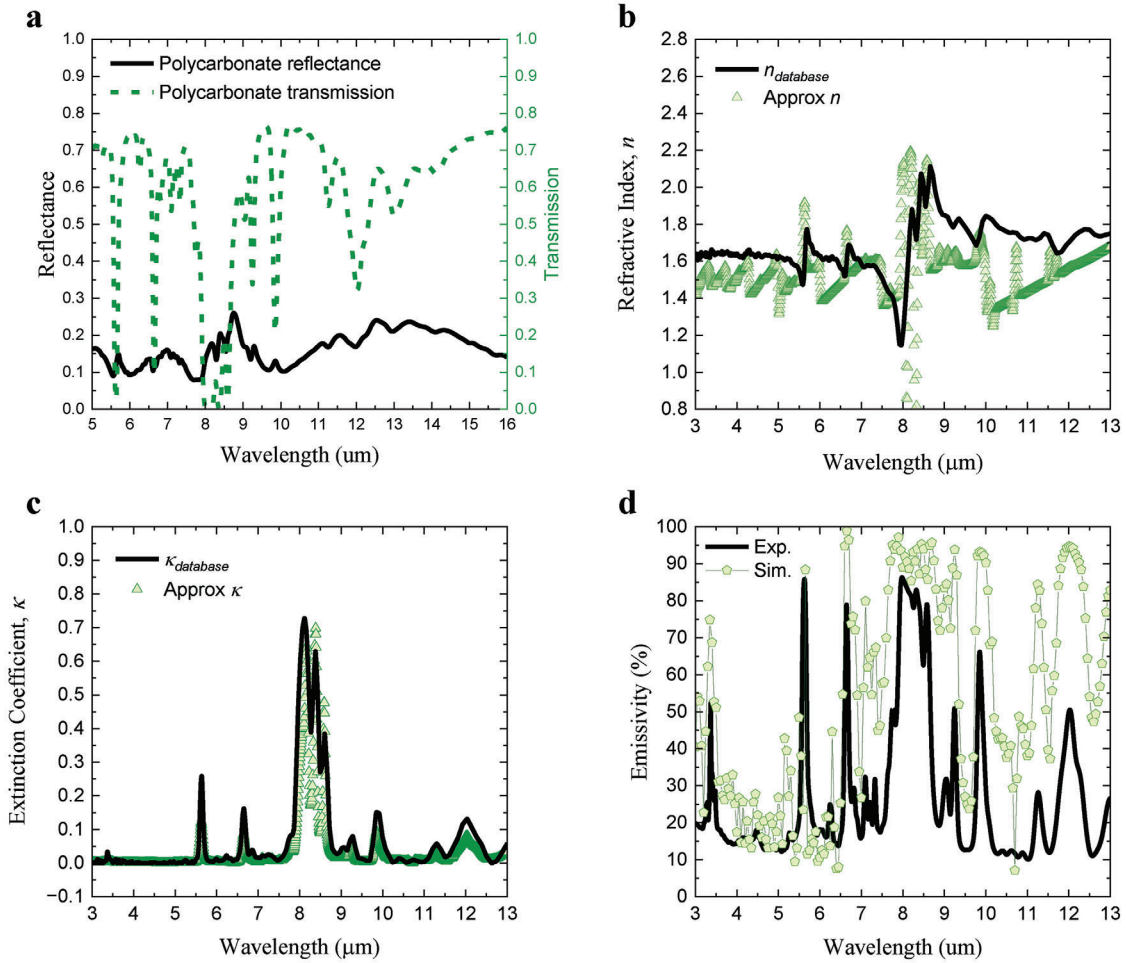

Figure 8. a) Optical characterization of reflectance and transmission spectra of a porous polymer film of polycarbonate with a thickness of 0.1 μm. First approach to the mid-IR b) refractive index and c) extinction coefficient spectra of the polycarbonate provided by the theoretical approximation along with the reference spectra. d) Simulation of the emissivity spectrum using this approach to n and κ spectra with COMSOL software, along with the experimental measurement.

compared to the reference spectra, whereas the first approach for κ shows a large error between 7 and 11 μm, where the reference remains close to zero and the approach found a different solution ≈0.6. However, it is worth noting that the uncertainty in this region of κ has little impact when the emissivity spectrum is simulated by COMSOL software (see Figure 7d). The simulation succeeds in reproducing the behavior of the experimental data.

Figure 8 shows the analysis of a porous polymer film of polycarbonate with a thickness of 0.1 μm.

This polymer film has an average mid-IR reflectance ≈0.15, with tiny oscillations between 0.05 and 0.25 from 5 to 16 μm (see Figure 8a). The transmission spectrum has several absorption bands, presenting a challenge to the model. The refractive index from the WVASE software database shows complex behavior, and while the main peaks in the reference spectrum are consistent with the approached n spectrum (the main peaks at 5.8, 6.8, 8.0, and 10.0 μm in the reference spectrum), further analysis is required for greater accuracy. The approached κ shows a good agreement with the reference spectrum. The simulated emissivity spectrum (Figure 8d) compares favorably with experimental data, providing a first qualitative approximation despite some noise and shift.

Figure 9 shows the analysis of a non-porous polymer film of polyethylene terephthalate (PET) without nanopores. The PET film thickness is ≈100 μm and the surface roughness is ≈7.2 nm.

The average reflectance of the PET film is ≈0.1, with a significant amount of noise observed in the spectra. Meanwhile, the transmission spectra reveal two regions where T > 0.6, first, between 2.5 and 5.5 μm, and second, between 14.5 and 16 μm. Additionally, there is a highly absorption region in the mid-IR range, between 7 μm and 10 μm, where transmission is nearly zero.

This information is used as input data in the theoretical approximation to obtain the n and κ spectra of the PET film, that are shown in Figure 7b,c in blue squares. As there is no data available to compare these results, the same PET film was analyzed by IRSE ellipsometry. The imaginary component of the complex dielectric function of PET film was modeled using a linear combination of 16 Gaussians oscillators (*GenOsc* layers) to fit all the

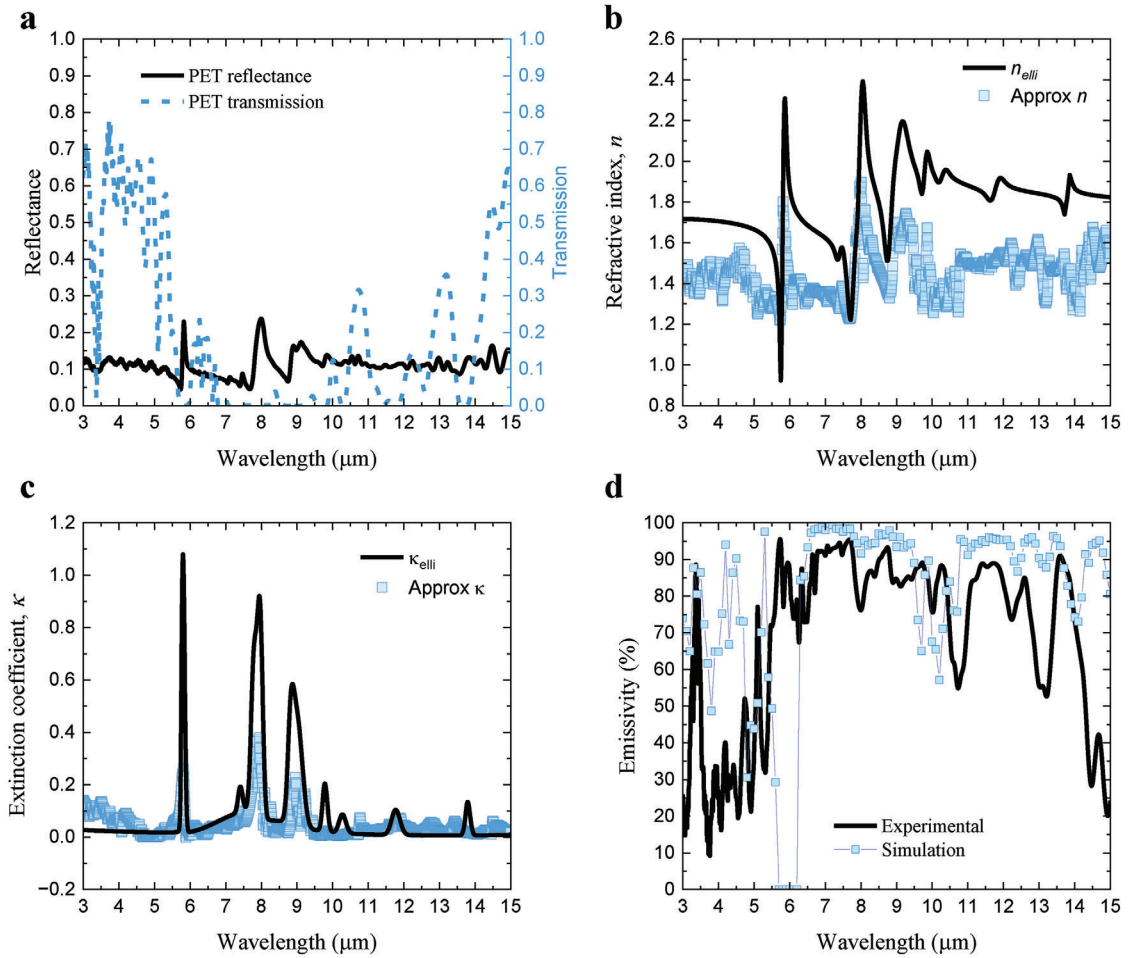

Figure 9. a) Optical characterization of reflectance and transmission spectra of a non-porous polymer film of polyethylene terephthalate (PET) with a thickness of 100 μm. First approach to the mid-IR b) refractive index and c) extinction coefficient spectra of the PET provided by the theoretical approximation along with the ellipsometric analysis. d) Simulation of the emissivity spectrum using the approached n and κ spectra with COMSOL software, along with the experimental measurement.

spectra. Then, the Kramers-Kronig integration formula is used to calculate the real part of the complex dielectric function. The n and κ spectra obtained by this ellipsometric analysis are shown in Figure 9b,c in black solid lines.

Comparing both approaches to the n and κ spectra, the main structure is common. However, the approximated n spectrum shows a noisier behavior and a shift is observed. In relation to the approximated κ spectra, the main peaks can be observed at 6, 8, and 9 μm, but the intensity is lower. These differences can be attributed to the noisy and low reflectance of this polymer, the surface roughness, and the thin thickness, which causes a significant back reflection.

As discussed above for the polycarbonate film, these challenging materials reveal the limits of the model. When the approached n and κ spectra are used to simulate the emissivity spectrum of a PET film, the results describe the complex behavior qualitatively, but further analysis is required to obtain a quantitatively accurate simulation. However, this information is useful to get an initial overview when characterizing a new material.

4. Conclusion

This study delves into the analysis of the mid-IR (3– 0 μm) complex refractive index of Anodic Aluminum Oxide (AAO) nanostructures anodized in four different electrolytes. Two methodologies were employed: first, Infrared Spectroscopic Ellipsometry (IRSE), and second, by theoretical modeling grounded on multilayer reflection and effective medium.

The refractive index (n) and the extinction coefficient (κ) of the AAO nanostructures were derived under four different anodization conditions to examine the impact of the morphology and the chemical structure on the optical parameters. It was found that the extinction coefficient was influenced by the different ions incorporated inside AAO due to the use of different electrolytes during anodization, while minor variations were observed in the refractive index. The alterations in κ spectra correspond with different absorptions bands, which influence the emissivity in the mid-IR wavelength range. The maximum values of κ are observed between 13 and 14 μm, reaching 1.30, 1.24, 1.13, and 1.09 for the AAO nanostructures anodized in phosphoric acid, oxalic acid,

sulphuric acid, and ethylene glycol containing sulphuric acid, respectively. Even if these changes are small, their impact on IR applications is significant and it is important to take them into account.

When comparing the n and κ obtained by several approaches (ellipsometric analysis and theoretical approximation), a significant agreement is achieved. Therefore, the proposed theoretical approximation offers a quick and efficient outline of the mid-IR complex refractive index using solely the thickness value and the reflectance and transmission spectra of a material. These calculations prove useful to obtaining an initial and reliable approach to n and κ spectra, as demonstrated for AAO nanostructures. The limits of this approach have been explored by analyzing a sapphire (a transparent metal oxide in the visible), a polycarbonate film (a porous polymer membrane used in for example medical applications), and a polyethylene terephthalate (PET) film (a non-porous polymer film, which is the most common thermoplastic polymer resin which is used in for example fibres for clothing, containers for liquids and foods). Both polymers exhibit complex optical behavior as they are active in the mid-IR, challenging the theoretical approximation. The results show a useful qualitative description when compared with the experimental data.

Lastly, the mid-IR emissivity spectra of the AAO nanostructures on Al foil were modeled using WVASE software and COMSOL software. The application of the previously derived n and κ spectra of free-standing AAO nanostructures resulted in a good agreement with the experimental measurement. This study encourages the development of new simulations and models to explore promising micro and nano-optical materials for use in mid-IR applications.

Supporting Information

Supporting Information is available from the Wiley Online Library or from the author.

Acknowledgements

C.V.M. acknowledges financial support from "Atracción de Talento Investigador" de la Comunidad de Madrid, contract 2019-T1/IND-13541. The authors acknowledge the service from the MiNa Laboratory at IMN, and funding from CM (project SpaceTec, S2013/ICE2822), MINECO (project CSIC13-4E-1794), and EU (FEDER, FSE). This study was partially supported by the Spanish Ministry of Science under project OMNIPATH (reference PID2020-119587RB-I00. I.C. acknowledges the funded by Formación de Profesorado Universitario (FPU) grant from the Spanish Ministry of Universities, reference FPU21/03180. M.M.G. acknowledged the Ministerio de Ciencia e Innovación with the Merge Project (PID2020118430GB-I00). We acknowledge support of the publication fee by the CSIC Open Access Publication Support Initiative through its Unit of Information Resources for Research (URICI).

Conflict of Interest

The authors declare no conflict of interest.

Author Contributions

M.M.G. and C.V.M. conceived the presented idea. A.D.L. developed the preparation of the samples and did the SEM characterization, and the FT-IR optical characterization. A.D.L. and E.B. performed the IRSE measurements and analysis. I.C.F and D.R. developed the theoretical model. A.D.L., E.B., I.C.F., D.R., M.M.G., and C.V.M. discussed the results and wrote the final manuscript. All authors have read and agreed to the published version of the manuscript.

Data Availability Statement

The data that support the findings of this study are available from the corresponding author upon reasonable request.

Keywords

anodic aluminum oxide (AAO), complex refractive index, FT-IR spectrophotometry, Infrared Spectroscopic Ellipsometry (IRSE), simulations

Received: July 24, 2024
Revised: November 12, 2024
Published online: December 16, 2024

[1] J. Grabska, K. B. Beć, C. W. Huck, *Comprehens. Analyt. Chem.* **2022**, *98*, 45.
[2] A. Skulteti, A. Kereszturi, M. Szabo, Z. Kereszty, F. Cipriani, *Planet. Space Sci.* **2020**, *184*, 104855.
[3] R. Shankar, M. Lončar, *Nanophotonics* **2014**, *3*, 329.
[4] D. Marris-Morini, V. Vakarin, J. M. Ramirez, Q. Liu, A. Ballabio, J. Frigerio, M. Montesinos, C. Alonso-Ramos, X. Le Roux, S. Serna, D. Benedikovic, D. Chrastina, L. Vivien, G. Isella, *Nanophotonics* **2018**, *7*, 1781.
[5] Y. Chen, Y. Francescato, J. D. Caldwell, V. Giannini, T. W. W. Maß, O. J. Glembocki, F. J. Bezares, T. Taubner, R. Kasica, M. Hong, S. A. Maier, *ACS Photonics* **2014**, *1*, 718.
[6] F. Désévédavy, C. Strutynski, A. Lemière, P. Mathey, G. Gadret, J.-C. Jules, B. Kibler, F. Smektala, *J. Am. Ceram. Soc.* **2020**, *103*, 4017.
[7] R. Anty, M. Morvan, M. Le Corvec, C. M. Canivet, S. Patouraux, J. Gugenheim, S. Bonnafous, B. Bailly-Maitre, O. Sire, H. Tariel, *JHEP Rep.* **2019**, *1*, 361.
[8] I. M. Pavlovetc, K. Aleshire, G. V. Hartland, M. Kuno, *Phys. Chem. Chem. Phys.* **2020**, *22*, 4313.
[9] J. Niu, Y. Wang, X. Zou, Y. Tan, C. Jia, X. Weng, L. Deng, *Appl. Mater. Today* **2021**, *24*, 101073.
[10] M. Ö. Korukçu, M. Kilic, *Int. Commun. Heat Mass Transfer* **2009**, *36*, 872.
[11] H. Wiggenhauser, *Infrared Phys. Technol.* **2002**, *43*, 233.
[12] P. Löper, M. Stuckelberger, B. Niesen, J. Werner, M. Filipič, S.-J. Moon, J.-H. Yum, M. Topič, S. De Wolf, C. Ballif, *J. Phys. Chem. Lett.* **2015**, *6*, 66.
[13] S. Fan, W. Li, *Nat. Photonics* **2022**, *16*, 182.
[14] Y. Wu, H. Zhao, H. Sun, M. Duan, B. Lin, S. Wu, *Energy Convers. Manage.* **2022**, *265*, 115768.
[15] A. P. Raman, M. A. Anoma, L. Zhu, E. Rephaeli, S. Fan, *Nature* **2014**, *515*, 540.
[16] N. D. Miranda, R. Renaldi, R. Khosla, M. D. McCulloch, *Renew. Sustain. Energy Rev.* **2021**, *149*, 111406.
[17] C. Sui, P.-C. Hsu, *ACS Energy Lett.* **2024**, *9*, 2997.
[18] J. Liang, J. Wu, J. Guo, H. Li, X. Zhou, S. Liang, C.-W. Qiu, G. Tao, *Natl. Sci. Rev.* **2023**, *10*, nwac208.
[19] G. A. Kumar, K. Ajay, *J. Nanophoton.* **2020**, *14*, 030901.
[20] I. Kousis, A. L. Pisello, *Adv. Opt. Mater.* **2023**, *11*, 2300123.
[21] Y. Cui, X. Luo, F. Zhang, L. Sun, N. Jin, W. Yang, *Particuology* **2022**, *67*, 57.

[22] X. Chen, M. He, S. Feng, Z. Xu, H. Peng, S. Shi, C. Liu, Y. Zhou, *Opt. Mater.* **2021**, *120*, 111431.
[23] Y. Gao, X. Song, P. Zhang, *Sol. Energy Mater. Sol. Cells* **2023**, *250*, 112081.
[24] B. Xiang, R. Zhang, Y. Luo, S. Zhang, L. Xu, H. Min, S. Tang, X. Meng, *Nano Energy* **2021**, *81*, 105600.
[25] B. Li, B. Cao, R. Song, Y. Zhong, C. Chen, H. Hu, S. Wu, Z. Xia, *J. Photon. Energy* **2023**, *13*, 015501.
[26] J. Zhao, Q. Meng, Y. Li, Z. Yang, J. Li, *ACS Appl. Mater. Interfaces* **2023**, *15*, 47286.
[27] A. Díaz-Lobo, M. Martin-Gonzalez, Á. Morales-Sabio, C. V. Manzano, *ACS Appl. Opt. Mater.* **2024**, *2*, 980.
[28] C. V. Manzano, A. Díaz-Lobo, M. Gil-García, Ó. Rodríguez de la Fuente, Á. Morales-Sabio, M. Martin-Gonzalez, *Adv. Opt. Mater.* **2024**, *12*, 2400551.
[29] Y. Fu, J. Yang, Y. S. Su, W. Du, Y. G. Ma, *Solar Energy Mater. Solar Cells* **2019**, *191*, 50.
[30] D. Liu, Z. Xia, K. Shi, X. Jiang, Z. Yu, Z. Zhang, Z. Fang, L. Ding, Z. Meng, *Opt. Mater.* **2019**, *92*, 330.
[31] Z. Zhan, M. ElKabbash, Z. Li, X. Li, J. Zhang, J. Rutledge, S. Singh, C. Guo, *Nano Energy* **2019**, *65*, 104060.
[32] Y. Liu, S. Son, D. Chae, P.-H. Jung, H. Lee, *Sol. Energy Mater. Sol. Cells* **2020**, *213*, 110561.
[33] Y. Xie, Q. Lai, P. Guo, J. Tan, *Infrared Phys. Technol.* **2020**, *109*, 103438.
[34] Y. Zhou, Y. Liu, Y. Li, R. Jiang, W. Li, W. Zhao, R. Mao, L. Deng, P. Zhou, *Opt. Mater. Express* **2020**, *10*, 1641.
[35] D. Lee, M. Go, S. Son, M. Kim, T. Badloe, H. Lee, J. K. Kim, J. Rho, *Nano Energy* **2021**, *79*, 105426.
[36] B. Zhao, J. Liu, M. Hu, X. Ao, L. Li, Q. Xuan, G. Pei, *Renew. Energy* **2023**, *205*, 763.
[37] C. V. Manzano, G. Bürki, L. Pethö, J. Michler, L. Philippe, *J. Mater. Chem. C* **2017**, *5*, 1706.
[38] M. Muñoz Rojo, Y. Zhang, C. V. Manzano, R. Alvaro, J. Gooth, M. Salmeron, M. Martin-Gonzalez, *Sci. Rep.* **2016**, *6*, 19014.
[39] C. Frantz, A. Lauria, V. Manzano, C. Guerra-Nuñez, M. Niederberger, C. Storrer, J. Michler, L. Philippe, *Langmuir* **2017**, *33*, 12404.
[40] E. Bertero, C. V. Manzano, G. Bürki, L. Philippe, *Mater. Des.* **2020**, *190*, 108559.
[41] C. V. Manzano, O. Caballero-Calero, A. Serrano, P. M. Resende, M. Martín-González, *Nanomaterials* **2022**, *12*, 4430.
[42] H. Zhuo, F. Peng, L. Lin, Y. Qu, F. Lai, *Thin Solid Films* **2011**, *519*, 2308.
[43] L.-R. Zhao, J. Wang, Y. Li, C.-W. Wang, F. Zhou, W.-M. Liu, *Phys. B: Conden. Matter* **2010**, *405*, 456.
[44] I. Mínguez-Bacho, S. Rodríguez-López, A. Climent-Font, D. Fichou, M. Vázquez, M. Hernández-Vélez, *Microporous Mesoporous Mater.* **2016**, *225*, 192.
[45] S. Garabagiu, G. Mihailescu, *Mater. Lett.* **2011**, *65*, 1648.
[46] A. Ruiz-Clavijo, O. Caballero-Calero, M. Martín-González, *Nanoscale* **2021**, *13*, 2227.
[47] K. Yamamoto, A. Masui, *Appl. Spectrosc.* **1995**, *49*, 639.
[48] C.-P. E. Varsamis, *Appl. Spectrosc.* **2002**, *56*, 1107.
[49] Y. Gu, Y. Hu, X. Zhao, X. Chen, *J. Quant. Spectrosc. Radiat. Transfer* **2018**, *217*, 305.
[50] J. Luo, N. J. Smith, C. G. Pantano, S. H. Kim, *J. Non-Cryst. Solids* **2018**, *494*, 94.
[51] T. Bonnal, A. Belarouci, R. Orobtchouk, E. Prud'homme, S. Tadier, G. Foray, *SN Appl. Sci.* **2020**, *2*, 2070.
[52] C. V. Manzano, J. P. Best, J. J. Schwiedrzik, A. Cantarero, J. Michler, L. Philippe, *J. Mater. Chem. C* **2016**, *4*, 7658.
[53] I. Horcas, R. Fernández, J. M. Gómez-Rodríguez, J. Colchero, J. Gómez-Herrero, A. M. Baro, *Rev. Sci. Instrum.* **2007**, *78*, 013705.
[54] M. N. Polyanskiy, *Refractiveindex.info database of optical constants. Sci. Data* **2024**, *11*, 94.
[55] R. L. Kelly, *J. Opt. Soc. Am.* **1972**, *62*, 1336.
[56] G. A. Katsifis, N. Suchowerska, D. R. McKenzie, *Plasma Processes Polym.* **2022**, *19*, 2100241.
[57] E. Márquez, E. Blanco, J. M. Mánuel, M. Ballester, M. García-Gurrea, M. I. Rodríguez-Tapiador, S. M. Fernández, F. Willomitzer, A. K. Katsaggelos, *Product. Cientifica* **2024**, *14*, 1.
[58] J. K. Pradhan, D. Pratap, S. A. Ramakrishna, *Pramana- J. Phys.* **2021**, *95*, 46.